

Phase transitions and quantum effects in pore condensates: A path integral Monte Carlo study

J. Hoffmann and P. Nielaba

Department of Physics, University of Konstanz, 78457 Konstanz, Germany

(Received 24 July 2002; published 24 March 2003)

Lennard-Jones condensates in cylindrical pores are studied by path integral Monte Carlo simulations with particular emphasis on phase transitions and quantum effects. The pore diameter effect and the influence of the interaction strength between the cylinder wall and the adsorbate particles on the structures and the location of the phase boundaries is studied and the quantum effect on the phase diagram is quantified by path integral Monte Carlo simulations. In case of strong wall-particle interactions good qualitative agreement with recent experimental results for the freezing of Ar-pore condensates is found. Meniscus structures in the solid phase are obtained as well as unexpected condensate structures for the system with the lighter Ne-particles due to quantum delocalization effects. The quantum effect on the freezing temperature can be as large as 10% in these systems.

DOI: 10.1103/PhysRevE.67.036115

PACS number(s): 05.10.Ln, 02.70.Ss, 64.70.Fx, 64.70.Dv

I. INTRODUCTION

Phase transitions of pore condensates in nanopores (i.e., Vycor) have been investigated by experimental and theoretical methods recently [1–11], for a recent review see Ref. [12].

Materials properties of systems condensed into pores of nanometer length scales (i.e., Vycor, Gelsil) are different from those of bulk systems. Important reasons for these effects are the geometrical finite size effects (the atomistic material structure cannot be neglected), the interaction of the material with the surrounding “glass” matrix and the large interface contributions relative to the volume. Typical nanopore materials are Vycor and Gelsil. Vycor [13] can be obtained by a spinodal decomposition process of a glass melt with a large B_2O_3 fraction. Upon cooling this system demixes into a SiO_2 - and a B_2O_3 -rich phase, the latter can be removed by an acid resulting in a porous SiO_2 system. Gelsil is a nanopore that can be obtained by a sol-gel process: a fluid silica-alcoxid is dried and its structure can be modified by tempering. Typical pore diameters range from 2.5 nm (Gelsil) to 13 nm (Vycor).

Besides spinodal decomposition, phase transition temperature reductions have been studied for cylindrical nanopores with small diameters. Many aspects of the liquid-gas transitions in cylindrical pores have been analyzed, but only a little attention has been paid to the freezing transition and quantum effects have been neglected. In a recent paper Wallacher and Knorr [14] studied the melting and freezing of Ar in Vycor nanopores. Many interesting effects are observed and interesting freezing scenarios discussed in their work.

In order to bridge the gap in the theoretical analysis of the freezing and the quantum effects in condensates of noble gases in nanopores we present here a systematic study of Lennard-Jones condensates in well defined cylindrical pores. In this paper we analyze phase transitions of Lennard-Jones systems in nanopores by Monte Carlo (MC) simulations [15]. The phase diagram is determined for various pore radii. At low temperatures the effects of the pore radius and the strength of the wall-particle interaction on the solidification are studied. The translational degrees of freedom have been treated quantum mechanically by path integral Monte Carlo

(PIMC) techniques [16], which allows us to quantify the effect of the particle masses on the phase transitions, energies, and solid structures.

II. THE MODEL

We model the nanopore by a cylinder of radius R and length L , applying periodic boundary conditions and nearest image convention along the pore axis. For a schematic picture of the geometry see Fig. 1.

The interaction potential between two particles in the cylinder at positions \mathbf{r} and \mathbf{r}' is modeled by the Lennard-Jones potential, suitable for Ar and Ne systems,

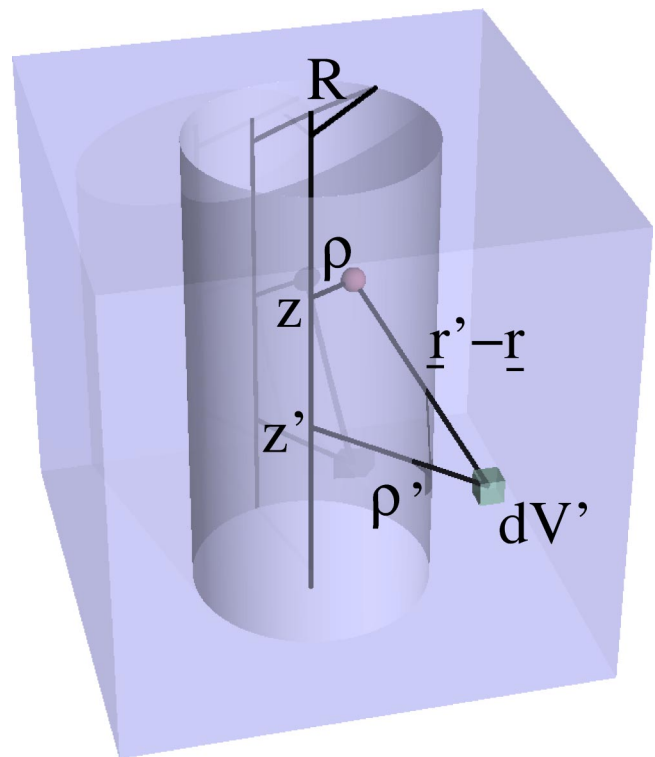


FIG. 1. Geometry of the system of a cylindrical pore with radius R .

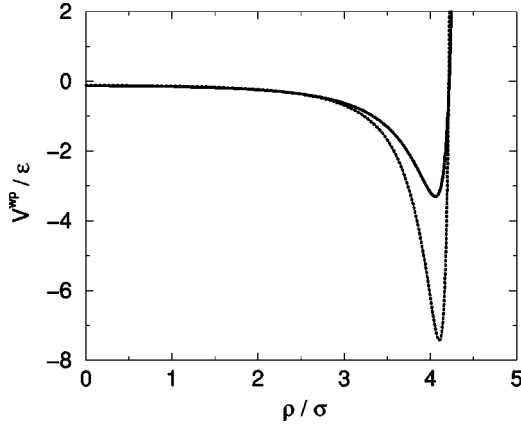


FIG. 2. Interaction potential V^{WP} between the wall of the cylinder and a particle at a distance ρ/σ from the cylinder axis. Full line, pore radius $R=5\sigma$, $\sigma^{WP}=1.094\sigma$, $\epsilon^{WP} n^W=0.9636\epsilon\sigma^{-3}$; dashed line, pore radius $R=4.75\sigma$, $\sigma^{WP}=0.75\sigma$, $\epsilon^{WP} n^W=7.07\epsilon\sigma^{-3}$.

$$V^{LJ}(|\mathbf{r}-\mathbf{r}'|)=4\epsilon\left[\left(\frac{\sigma}{|\mathbf{r}-\mathbf{r}'|}\right)^{12}-\left(\frac{\sigma}{|\mathbf{r}-\mathbf{r}'|}\right)^6\right] \quad (1)$$

with the particle ‘‘diameter’’ σ and the pair interaction energy ϵ . In order to get results comparable with earlier molecular dynamics simulations for the fluid condensates [17] the potential is cutoff and shifted at a cutoff radius $r_{\text{cut}}=2.5\sigma$. No tail corrections have been used.

The interaction between a particle at position \mathbf{r} in the cylinder and the surrounding of the cylinder is obtained by integrating the (not cutoff Lennard-Jones) interaction with parameters σ^{WP} and ϵ^{WP} to the particles in the volume V' outside the cylinder modeled as a homogenous system of particle density n_w (see Figs. 1 and 2),

$$V^{WP}(\mathbf{r})=\int_{V'} V^{LJ}(|\mathbf{r}'-\mathbf{r}|)n_w dV'. \quad (2)$$

In Fig. 2 we show the resulting potential $V^{WP}(\rho)$ as a function of the radial distance from the cylinder axis ρ for a pore with $R=5\sigma$ and two different sets of parameters. Since many of the studies presented below are made for the first parameter set in Fig. 2 we will refer to this case in the future as potential V_I^{WP} .

III. PATH INTEGRAL MONTE CARLO SIMULATIONS

Canonical averages $\langle A \rangle$ of an observable A in a system defined by the Hamiltonian $\mathcal{H}=E_{\text{kin}}+V_{\text{pot}}$ of N particles in a volume V are given by

$$\langle A \rangle=Z^{-1} \text{Tr}[A \exp(-\beta\mathcal{H})]. \quad (3)$$

Here $Z=\text{Tr}[\exp(-\beta\mathcal{H})]$ is the partition function and $\beta=1/k_B T$ is the inverse temperature. Utilizing the Trotter-product formula,

$$\exp(-\beta\mathcal{H})=\lim_{P\rightarrow\infty} [\exp(-\beta E_{\text{kin}}/P)\exp(-\beta V_{\text{pot}}/P)]^P, \quad (4)$$

TABLE I. Mass, Lennard-Jones parameters, and degeneracy temperature T_D at density $\rho=1/\sigma^3$ for Ar and Ne.

	Ar	Ne
m/amu	40	20
$\epsilon/k_B\text{K}$	121	35.8
$\sigma/\text{\AA}$	3.41	2.75
T_D/K	0.1	0.32
T_D^*	8.6×10^{-3}	9.0×10^{-2}

we obtain the path integral expression [16] for the partition function:

$$Z(N, V, T)=\lim_{P\rightarrow\infty} \left(\frac{mP}{2\pi\beta\hbar^2}\right)^{3NP/2} \prod_{s=1}^P \int d\{\mathbf{r}^{(s)}\} \times \exp\left[-\frac{\beta}{P} V_{\text{eff}}(\{\mathbf{r}^{(s)}\})\right] \quad (5)$$

with

$$V_{\text{eff}}(\{\mathbf{r}^{(s)}\})=V_{\text{pot}}(\{\mathbf{r}^{(s)}\})+\sum_{k=1}^N \frac{mP^2}{2\hbar^2\beta^2} (\mathbf{r}_k^{(s)}-\mathbf{r}_k^{(s+1)})^2. \quad (6)$$

Here, m is the particle mass, integer P is the Trotter number, and $\mathbf{r}_k^{(s)}$ denotes the coordinate of particle k at Trotter index s , and periodic boundary conditions apply, the particle with Trotter index $P+1$ is the same as the particle with Trotter index 1. This formulation of the partition function allows us to perform Monte Carlo simulations for increasing values of P approaching the true quantum limit for $P\rightarrow\infty$. Using $P=1$ the simulation will be completely classical, since Eq. (6) becomes the classical partition function. In contrast to the classical MC-simulation scheme, the particle mass m becomes important, since it influences the configurational part of Eq. (6). In this study the masses $m^*=m\sigma^2\epsilon/\hbar^2=1000(\hbar/\epsilon\sigma^2)$ and $m^*=100$ have been used well approximating the particle masses of argon ($m^*=1160$) and neon ($m^*=112$). The mass and the Lennard-Jones parameters for argon and neon are listed in Table I.

We note that in our PIMC simulations the effect of quantum statistics has been neglected. We carefully analyzed the amount of ‘‘overlapping’’ paths in our simulations and computed an estimate of the degeneracy temperature $T_D=\rho^{2/3}\hbar^2/mk_B$ as given by Ceperley [16] at a density $\rho\sigma^3=1$, which is far above the densities that have been identified as phase transition densities in our study. At this high density the probability for ‘‘overlapping’’ paths is highest and the resulting values for T_D are listed in Table I and give an upper bound for T_D at the densities used in our study. We note that these degeneracy temperatures are far below any temperature considered in this study. We are thus confident that quantum statistics will not have any effect on our results within the numerical accuracy and thus can be neglected in our PIMC simulations.

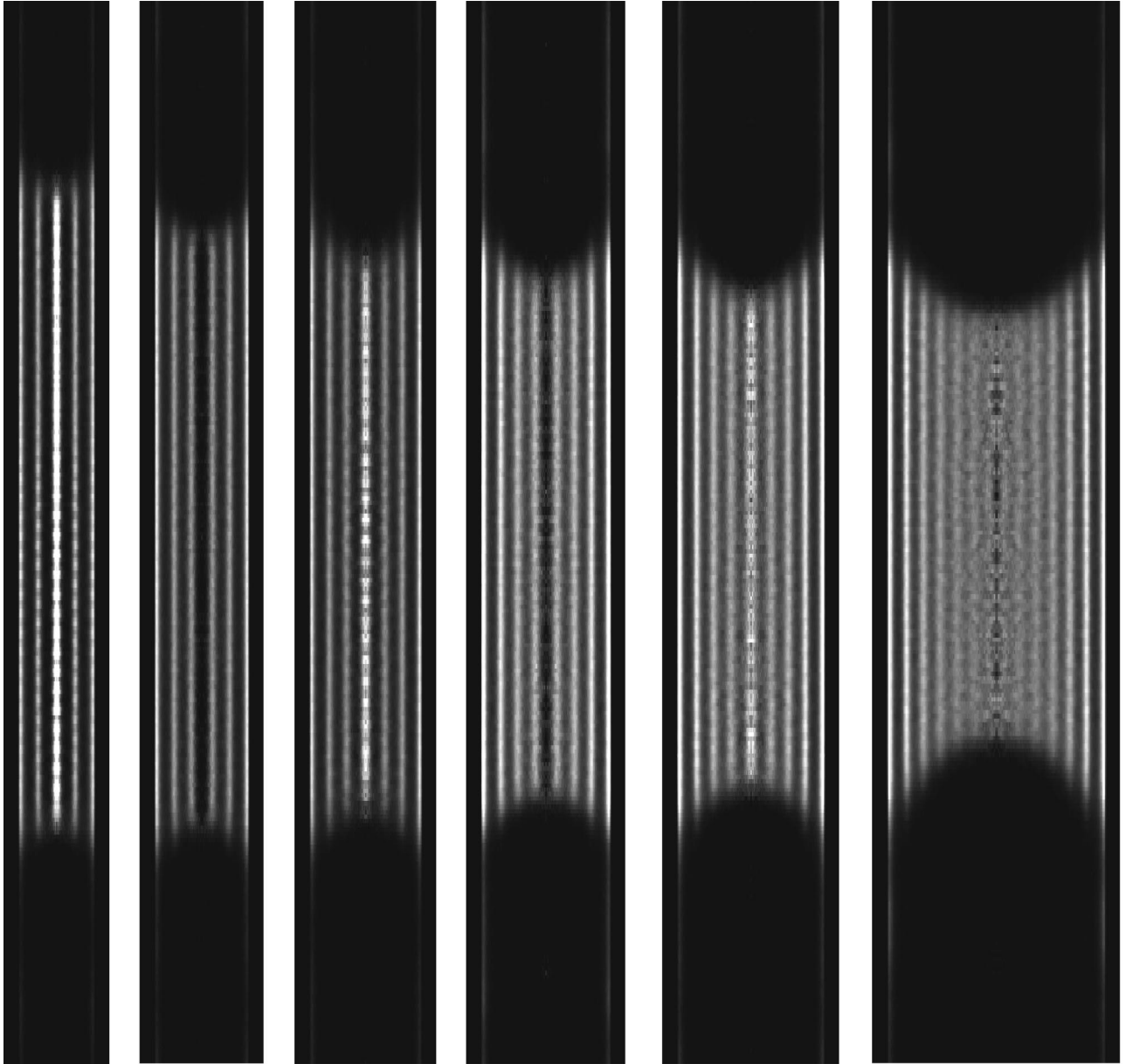


FIG. 3. Density distributions (cylindrical average) for classical LJ-pore condensates in cylindrical pores of length 60σ at $T^*=0.6$ with given pore radii and numbers of particles.

Thermal averages in the ensemble with constant pressure p are given via the corresponding partition function

$$\Delta(N, p, T) = \int_0^\infty dV(L) \exp[-\beta p V(L)] Z(N, V, T). \quad (7)$$

Thereby the volume is changed by varying the cylinder length L , the pore radius R is kept constant.

Typical system sizes are $N=1570$ Particles in $R=5\sigma$ pores and $N=300$ to 500 particles in $R=3\sigma$ pores using P values up to 128. To obtain a PIMC-data point in Fig. 20, 70 000 MC steps have been performed after an equilibration phase of 30 000 MC steps (in one MC-Step all NP particles have been subjected to a translational displacement). This requires about 3 to 3.5 CPU hours (single processor) on a

CRAY T3E-1200, a special parallel processing procedure was used (32 processors for P value 64) [18].

IV. RESULTS

A. Phase transitions

We have analyzed [19] many interesting properties of Lennard-Jones pore condensates recently (modeled as Lennard-Jones systems with particle diameter σ and interaction energy ϵ). These systems have—similar to the gas-liquid phase transition in the corresponding “bulk” systems—an adsorbate-condensate phase transition at low temperatures, the precise shape of the phase diagram is strongly influenced by the system geometry (pore radius). It turns out that with increasing attractive wall interaction the

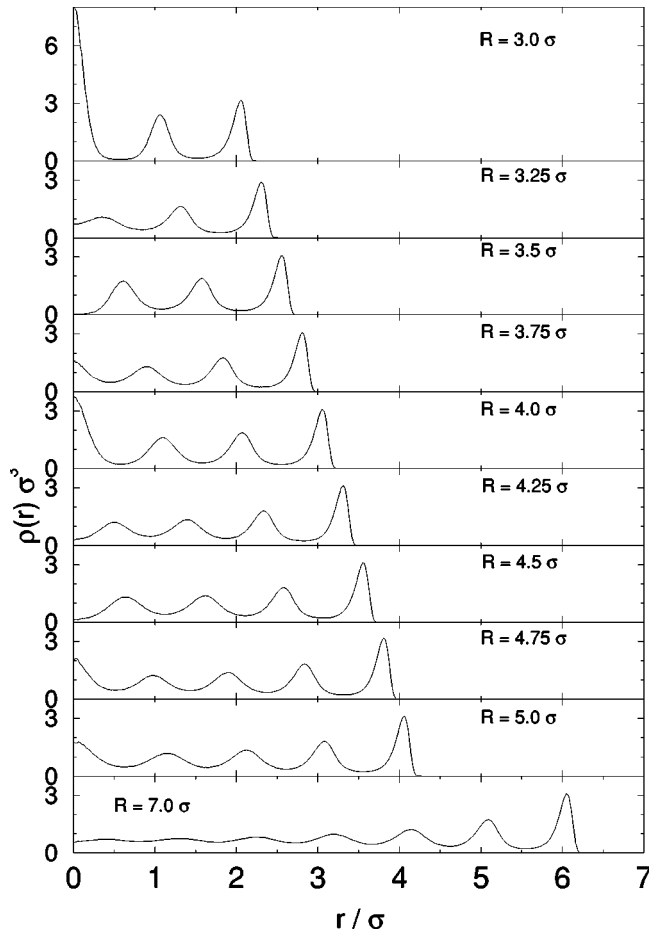


FIG. 4. Radial density distribution in the condensate (center part in Fig. 3); $T^* = 0.6$.

critical temperature T^* decreases, the critical density increases, the adsorbate density increases strongly, and the condensate density increases weakly. To calculate these densities MC simulations have been performed in the NVT [(particle number) \times volume \times temperature] ensemble at temperatures and densities in the coexistence region. For this choice of system parameters the system separates in an adsorbate and a condensate-phase. The coexistence densities are obtained by tracing the number of particles in 25 equidistant cylinder slices oriented perpendicular to the cylinder axis and by analysis of the resulting density histograms. The results are in perfect agreement with those calculated by evaluating the density profiles that have been obtained by averaging the number of particles in 250×250 annular bins over the simulation run.

The critical temperature T_c^* is reduced with decreasing pore diameter. Beginning from the wall a formation of layered shell structures is found which may allow or prevent the occupancy of sites at the pore axis due to packing effects.

In Figs. 3 and 4 we present the density profiles (cylindrical average) as well as the radial density distribution in the condensate (axial averages over the center parts of the systems in the Fig. 3). We note the layering structure and an oscillatory behavior of the density at the pore axis ($r=0$) as a function of pore radius with density maxima for pore radii

of $n\sigma$ and minima for pore radii of $(n+1/2)\sigma$. For large pore diameters the density oscillations decay from the wall towards the pore axis and the system approaches the “bulk” behavior.

A meniscus is formed with decreasing curvature for decreasing temperature (see Fig. 5) due to interfacial free energy minimization effects favoring linear interfaces at low temperatures. The configurations become less stable compared to the bulk system without interfaces and thus the critical temperature decreases.

B. Phase diagram of the 5σ pore

The phase diagram for the pore with radius $R=5\sigma$ and length $L=60\sigma$ obtained by a classical NVT simulation of 1570 particles ($n^*=0.333$) is shown in Fig. 6.

At temperatures $T^* > T_c^* = 0.9 \pm 0.25$ no phase separation is found. The critical density is located between $0.3\sigma^{-3}$ and $0.45\sigma^{-3}$. For $T^* < T_c^*$ the system separates into the adsorbate phase at low densities and the condensate phase at high densities. With decreasing temperature the adsorbate densities decrease, while the condensate densities increase. Tight above the triple point temperature almost all particles have joined the condensate phase. Below the triple point temperature T_t the condensed phase solidifies. Melting occurs at slightly higher temperatures, so a small hysteresis loop has been found due to metastable states near the triple point. The triple point temperature is located between the solidification and melting temperatures: $T_S < T_t < T_M$. In the fluid as well as in the solid phase we obtain a layering structure. In case of the fluid-solid phase transition a triangular lattice is formed in the layers in azimuthal direction, see Fig. 7.

This can be quantified by the order parameter Ψ_6 , which can be computed in the “unrolled” two-dimensional configuration of the outer layer. The order parameter Ψ_6 is defined as:

$$\Psi_6 = |\langle \exp(i6\phi_{kl}) \rangle|, \quad (8)$$

where ϕ_{kl} is the angle between $\mathbf{r}_l - \mathbf{r}_k$ of the neighbor particles k, l and an arbitrary but fixed reference direction, e.g., the pore axis direction.

The density jump at the triple point is accompanied by jumps in the Ψ_6 order parameter and the potential energy (Figs. 8 and 9).

The interface between the solid and the fluid phase is curved resulting in a meniscus structure. The meniscus curvature is reduced at lower temperatures, but is still present in the solid phase.

C. Freezing of the pore condensate

In Fig. 10 we present the freezing temperatures T_S for various systems, as a function of the pore radius as been found by the occurrence of a triangular lattice in the outer shell in single “cooling” runs. The freezing temperatures shown in Fig. 10 have been obtained in simulations by sequentially decreasing the temperature by an amount of $\Delta T^* = 0.01$ at a given pore diameter, the transition temperature shown in the figure is the first temperature at which a

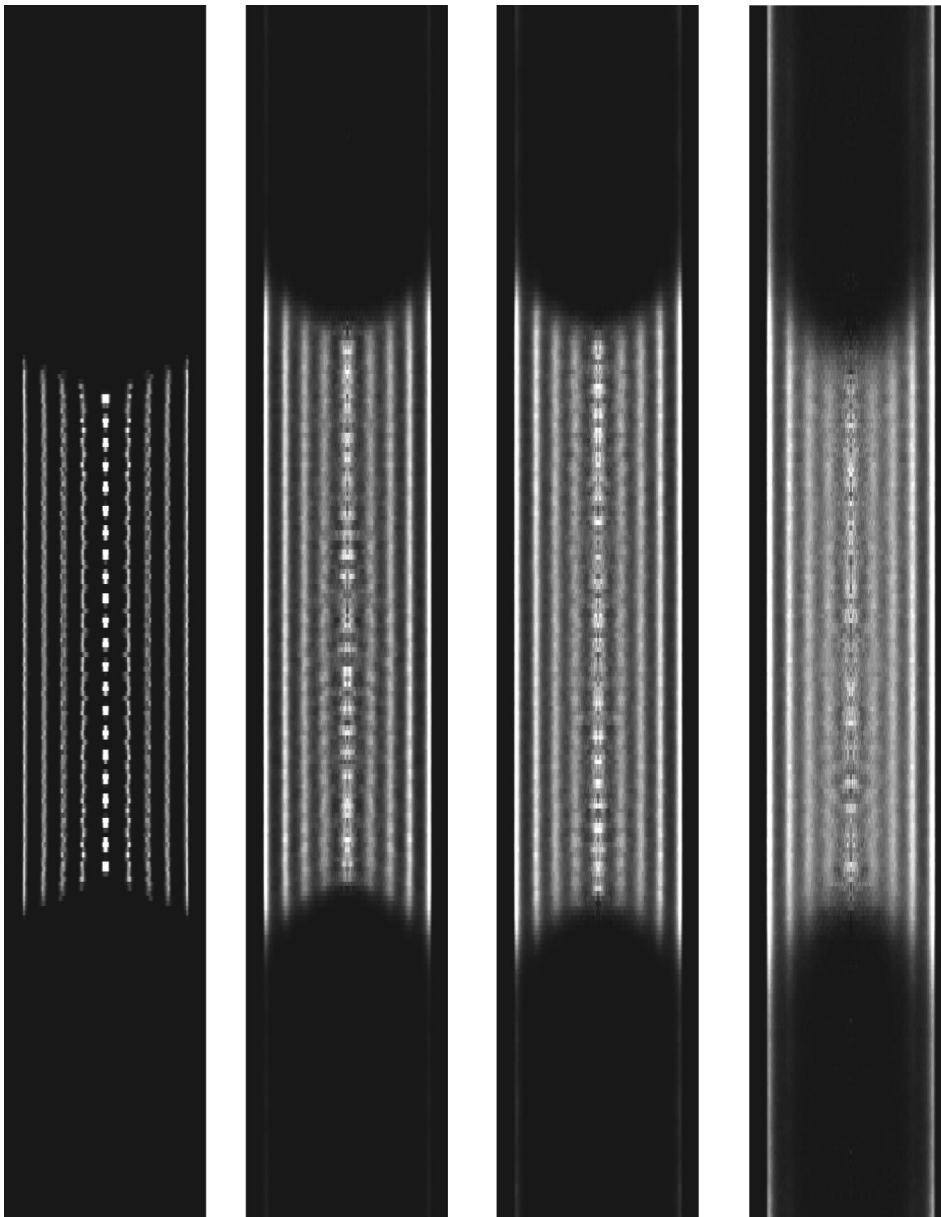


FIG. 5. Density distributions (cylindrical average) for 1570 classical LJ particles in a cylindrical pore of radius $R=5\sigma$ and length $L=60\sigma$ at $T^*=0.20, 0.55, 0.60, 0.75$ (from left to right).

frozen structure was found in this procedure. The resulting error for the freezing temperature is thus in the range of $\Delta T^*=0.01$ towards higher temperatures. The geometrical finite size effect of the pore radius results in a packing effect with preferential occupancy of sites at the pore axis for pores with radii 3.75σ and 4.75σ , whereas for radii of 3.25σ and 4.25σ the density at the axis is reduced. This may explain the destabilization of the system in case of the 3.25σ pore resulting in a small decrease of the freezing temperature compared to the other radii.

The triple point temperature is influenced by the geometrical finite size effects (pore radius) as well as by the wall-particle interaction. In Fig. 11 we note that with increasing interaction strength between the cylinder wall and the condensate particles T_S (indicated by the jump in the energy) is shifted to higher temperatures due to a stabilization of the solid structures at the cylinder wall.

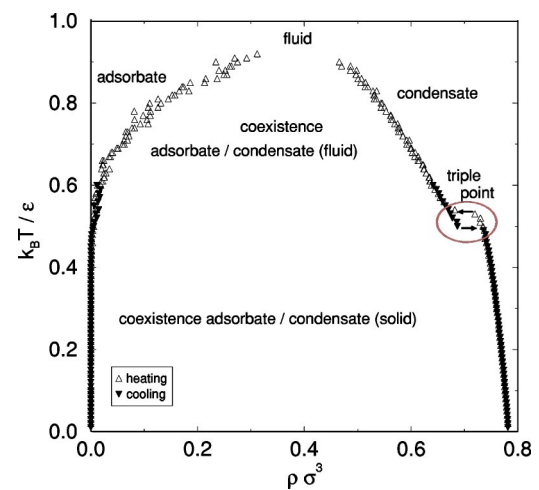


FIG. 6. Phase diagram of the classical LJ-pore condensate in a cylindrical pore with radius $R=5\sigma$, calculated at $\bar{n}^*=0.333$.

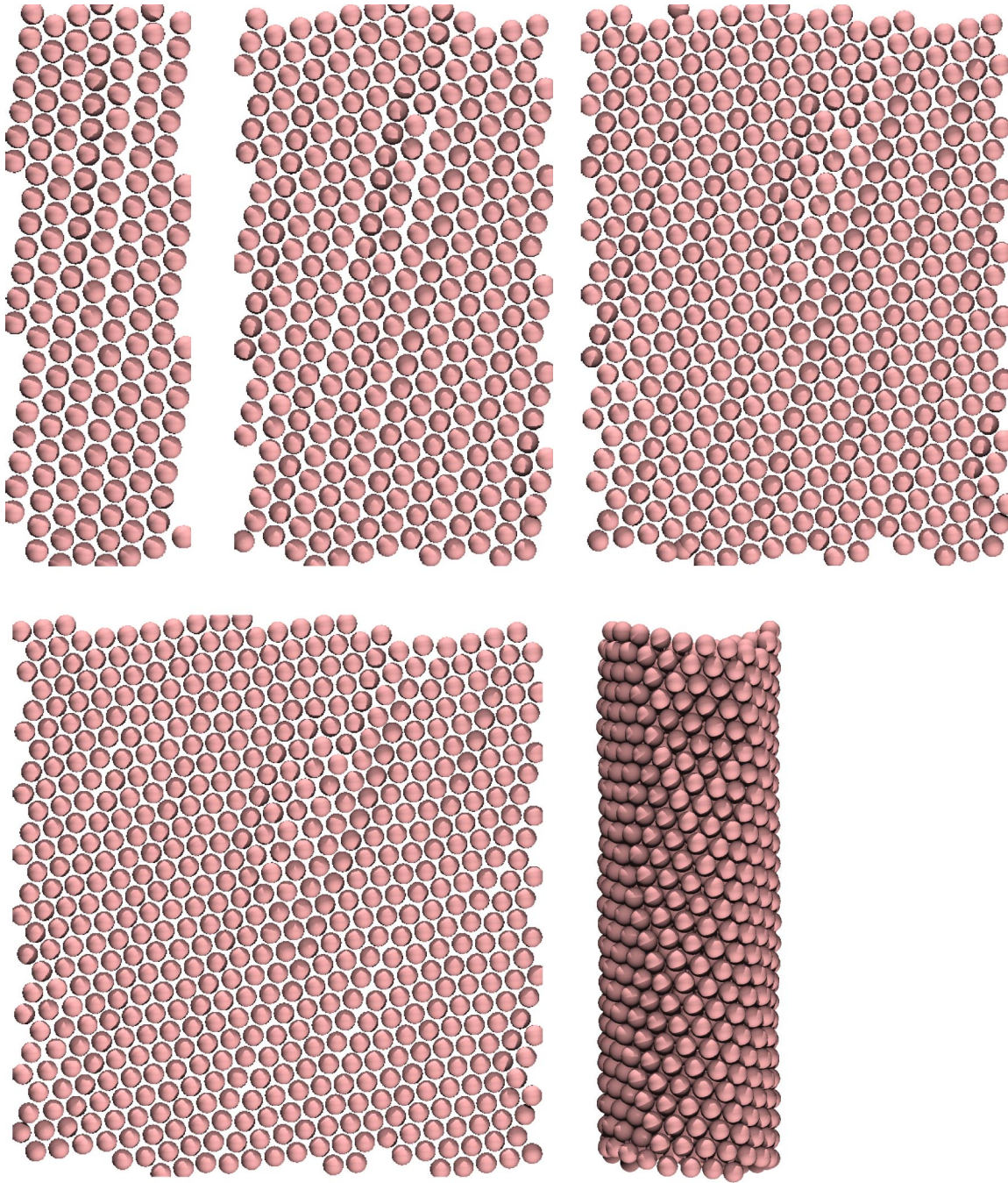


FIG. 7. Layer structure in a cylindrical pore of radius $R=5\sigma$ ($N=1570$, $L=60\sigma$) at $T^*=0.02$. From left to right: the four inner layers around the cylinder axis unrolled and a snapshot of the pore.

At sufficiently strong wall-particle interaction ($\epsilon^{WP} = 1.509\epsilon$, $\sigma^{WP} = 1.094\sigma$) we find a two step fluid-solid phase transition. In Fig. 12 we show typical configurations for a pore with radius $R=4\sigma$ at three temperatures. At $T^*=0.6$ the system is fluid, at $T^*=0.46$ the central condensate region is frozen and the adsorbate region is fluid, and at $T^*=0.2$ the adsorbate is frozen as well. The energy as a function of temperature is shown in Fig. 13.

At $T^*=0.575$ a solidification of the condensate phase is found by a jump in the energy. The condensate freezes in one piece from the cylinder wall to the axis. The remaining fluid

adsorbate phase solidifies only at $T^*=0.375$. The bond orientational order parameter of the outer layer is presented in Fig. 13. Indeed the two step “freezing” scenario is supported by these data as well. In Fig. 13 hysteresis effects are analyzed as well. Only a little effect on the values of Ψ_6 is found on heating or cooling the system.

A different scenario was found for even stronger interactions between the wall and the particles. For potential parameters as given in Fig. 2 (dashed line) we find the following freezing scenario. The system freezes at the cylinder wall due to the strong binding energy to the wall (see Fig. 14 for

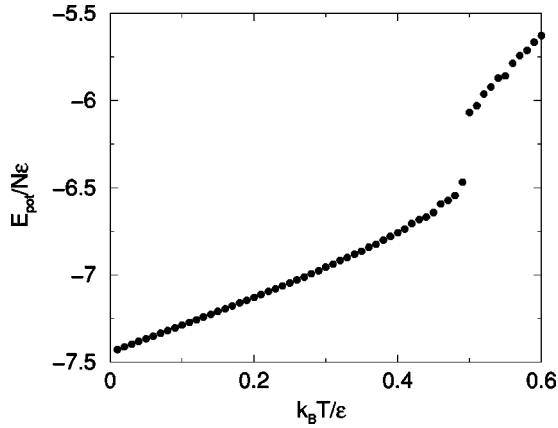


FIG. 8. The potential energy of a classical LJ condensate in a cylindrical pore with radius $R = 5\sigma$ versus temperature. Parameters as in Fig. 5.

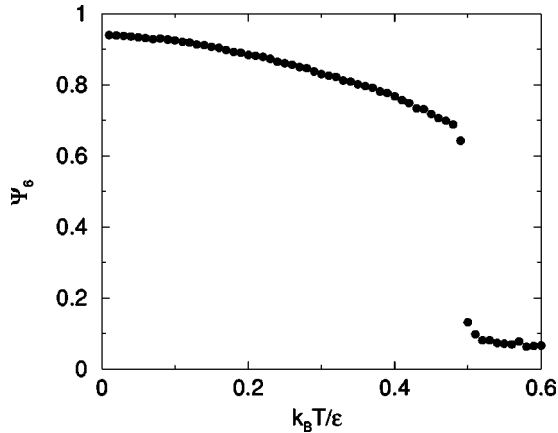


FIG. 9. The bond orientational order parameter Ψ_6 in azimuthal direction (outer layer) of a classical LJ condensate in a cylindrical pore with radius $R = 5\sigma$ versus temperature. Parameters as in Fig. 5.

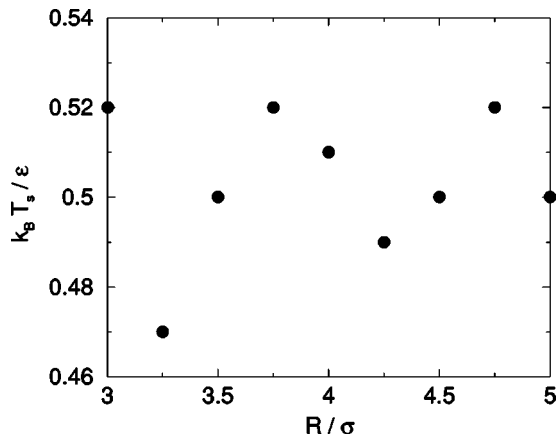


FIG. 10. Freezing temperature T_s for different pore radii, as found by the occurrence of a triangular lattice in the outer shell in single cooling runs. Parameters as in Fig. 3. For error bars see text.

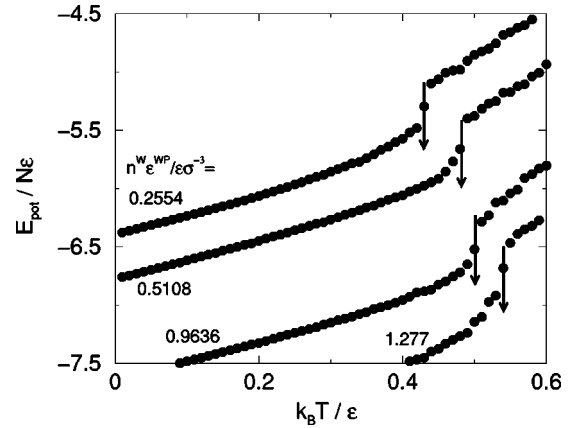


FIG. 11. Potential energy versus temperature for different interaction strengths between the cylinder wall and the adsorbate particles. Arrows indicate the phase transition temperatures. ($R = 4\sigma$, $L = 60\sigma$, $N = 1005$.)

typical configurations and density distributions and Fig. 15 for radial distribution functions). Between the layer at the cylinder wall and the next layer only a very small particle exchange is found as can be seen in the sharp decrease of the radial distribution function for ρ/σ values between 3 and 4 in Fig. 15.

The region close to the cylinder axis, however, is still fluid and freezes only at lower temperatures. The different behavior of layerwise freezing in systems with strong wall-particle interaction and the blockwise freezing for small particle-pore interactions can be understood as follows: particles in the second layer can be treated as particles in a pore with radius $R^{\text{eff}} = R - \sigma$ with a potential consisting of the particle-wall potential and the particle-particle potential to the particles in the first layer. Latter is in the order of 3ϵ since there are three nearest neighbors in the first layer. The effective outer potential for the second layer is in the same order as the outer potential for particles in the first layer for systems with small wall-particle interactions such as for the solid line in Fig. 2. For even stronger wall-particle potential—such as the dashed line—the effective outer potential for the inner layers differs from the potential of the outer layer.

Such two stage freezing phenomena were observed in experiments of melting and freezing of Ar in Vycor pores recently [14].

For small pore radii and not too small wall-particle interactions we observe a layering structure of the condensate. For a bulk system instead one would expect a crystalline fcc or hcp structure. In agreement with this, for large pore diameters and not too strong wall-particle interactions indeed no layering structure is found. In this case structures are formed with local fcc or hcp order. The membership of a particle to the lattice structures is decided by the symmetry properties of its nearest neighbors. In case of the fcc structure the neighborhood of a particle has point symmetry in contrast to the case of the hcp structure. Figure 16 shows the different regions with local fcc and hcp structure of a simulation in the $N-p-T$ ensemble at $p = 0$ and $k_B T/\epsilon = 0.15$.

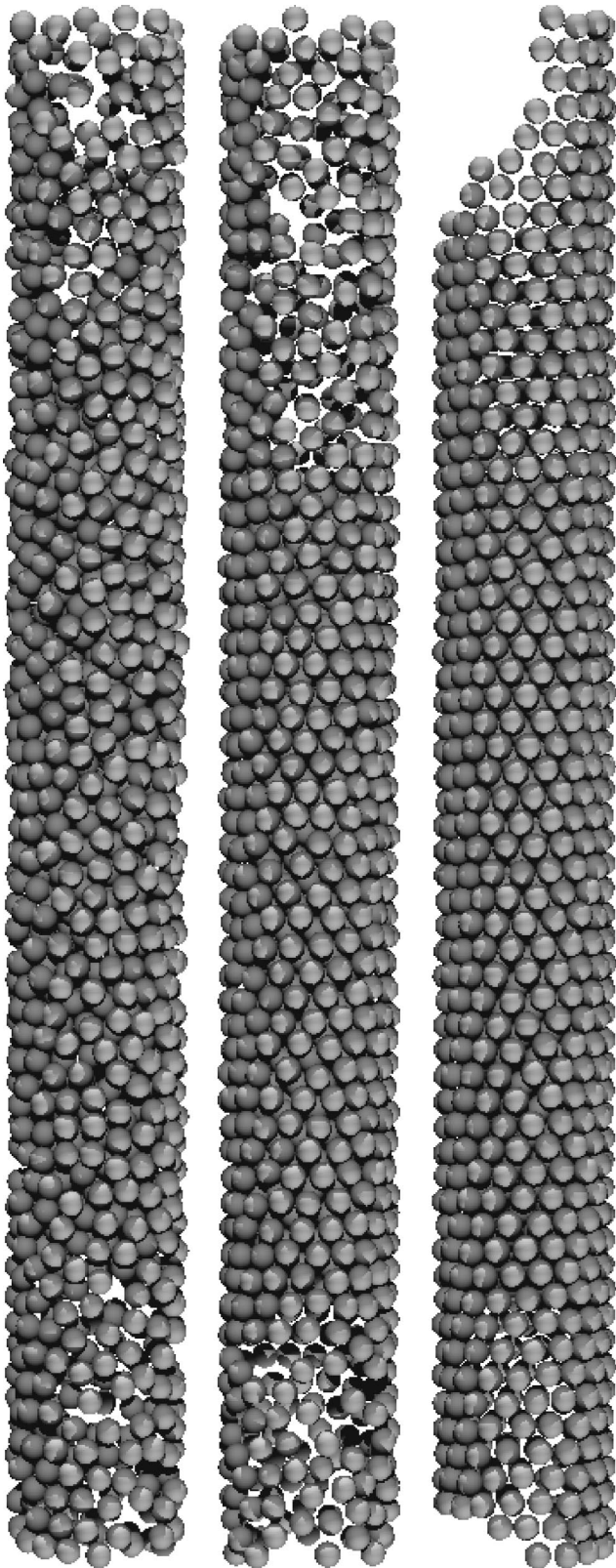


FIG. 12. Configurations of classical LJ condensates ($N = 1500$) in a cylindrical pore of radius $R = 4\sigma$, and length $L = 60\sigma$ at $T^* = 0.6, 0.46, 0.2$ (from left to right). The potential parameters for the wall-particle interactions are: $\sigma^{WP} = 1.094\sigma$, $\epsilon^{WP} n^W = 1.5092\epsilon\sigma^{-3}$.

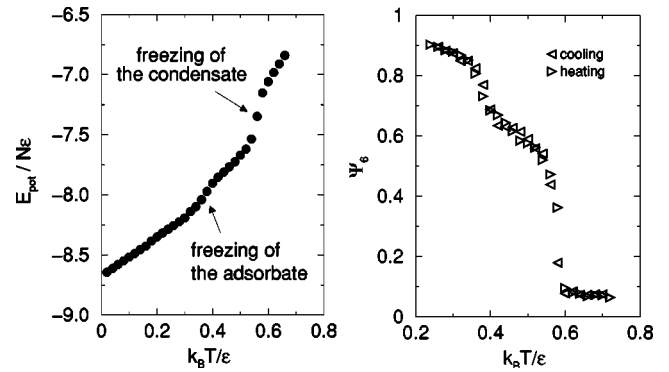


FIG. 13. Potential energy of a classical LJ condensate and bond orientational order parameter for the outer layer versus temperature in a cylindrical pore of radius $R = 4\sigma$. Parameters as in Fig. 12.

D. Quantum effects

At low temperatures quantum effects become important which have been ignored in most of the existing theoretical studies of pore condensates.

By PIMC simulations [20–23] we have investigated the effect of the quantum mechanics on the system properties as a function of the temperature. In contrast to classical MC simulations we obtain by PIMC simulations for Ar and Ne condensates a horizontal temperature dependence of the potential energy resulting in a decrease of the specific heat to zero at small temperatures in agreement with the third law of thermodynamics, see Fig. 17.

At very low temperatures the proper approach to the quantum limit requires large Trotter orders. This limits the range of accessible temperatures by PIMC.

The effect of quantum mechanics on the bond orientation order parameter of the outer layer is shown in Fig. 18.

The phase transition to the ordered solid is shifted by about 10% to lower temperatures for $m^* = 100$, and a reduction of the order parameter at very low temperatures by about 10% is found as well. These effects can be attributed to the ground state oscillations of the light particles around their lattice sites destabilizing the perfect triangular structure of the outer layer.

The average mean square deviation of a condensate particles z coordinate from its average value is shown in Fig. 19.

The values for the classical system approach zero for low temperatures since the particles are well localized on lattice sites. In quantum simulations, however, the low temperature limit is different from zero due to ground state fluctuations at low temperatures. This effect increases with decreasing particle masses as can be seen in Fig. 19.

The quantum effect on the phase boundaries in the phase diagram is shown in Fig. 20.

For $m^* = 1000$ quantum effects become important below $T^* = 0.2$. For $m^* = 100$ quantum effects are large already at temperatures close to the critical temperature. T_c is reduced by 10% and the density of the solid condensate is strongly reduced.

Other significant quantum effects can be found in the particle ordering in the solid pore condensate at low temperatures, see Fig. 21.

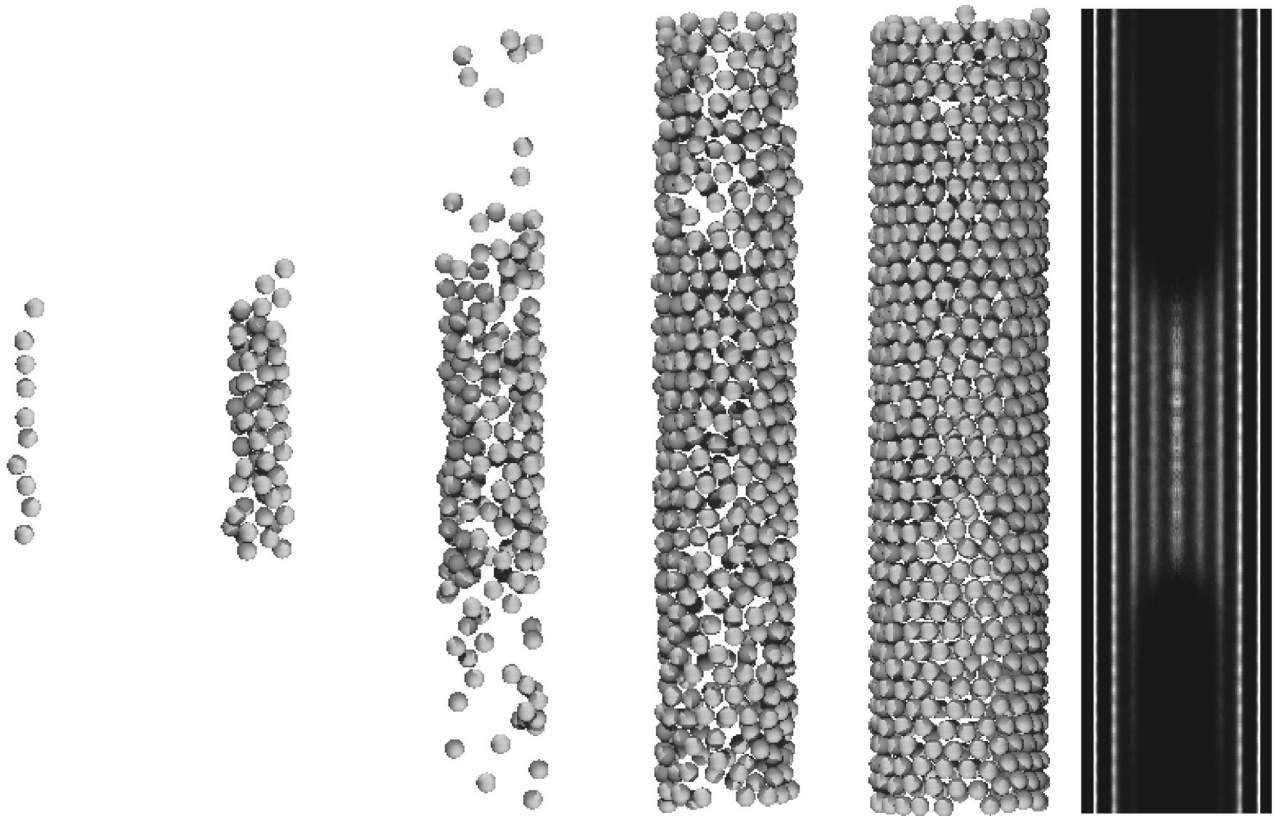


FIG. 14. Left, configurations in radial layers of a classical LJ condensate in a cylindrical pore (1770 particles) with radius $R=4.75\sigma$ and length $L=60\sigma$ at $T^*=0.64$ and strong wall-particle interaction (with potential parameters as given in Fig. 2 for the dashed curve). The particles in the layers around the cylinder axis show an ordered solid structure at the wall and a disordered structure in the radial region around the cylinder axis. Right picture, density distributions (cylindrical average).

The classical simulation and the PIMC simulation for $m^*=1000$ results in similar structures, in particular for a pore radius of $R=3.25\sigma$ the density on the cylinder axis is very low. This, however, is very different for the structures with $m^*=100$, where the density on the cylinder axis is

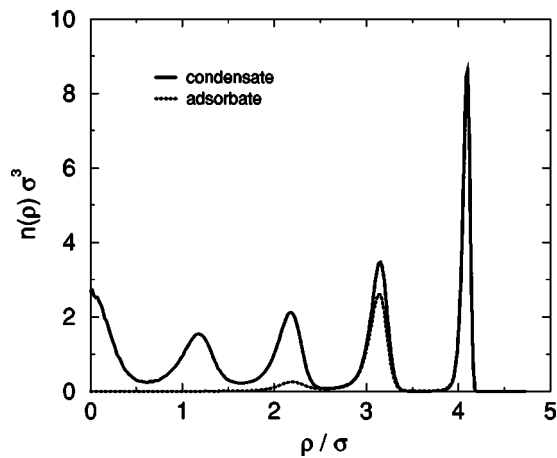


FIG. 15. Radial distribution functions for the system with parameters of Fig. 14. The condensate region is the center region of Fig. 14 (1/5 of the cylinder length), the adsorbate is taken from the regions at the top and at the bottom (1/5 of the cylinder length each) of the system in Fig. 14.

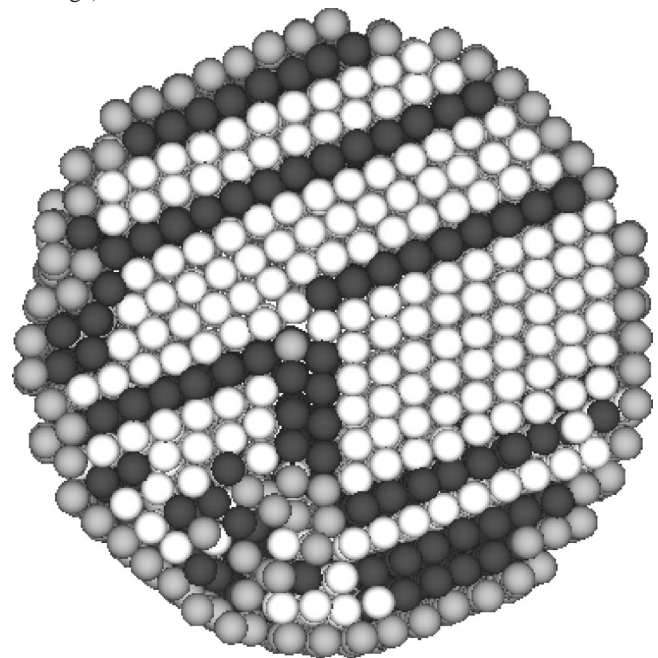


FIG. 16. Solid condensate (3000 LJ particles) in a cylindrical pore of radius $R=10\sigma$ at $T^*=0.15$ and $p=0$ ($N-p-T$ ensemble). Interaction potential parameters for the wall-particle interaction: $\sigma^{WP}=1\sigma$, $\epsilon^{WP}n^W=0.5\epsilon\sigma^{-3}$. Black particles: local hcp symmetry, white particles, local fcc symmetry, gray particles, not having either symmetry.

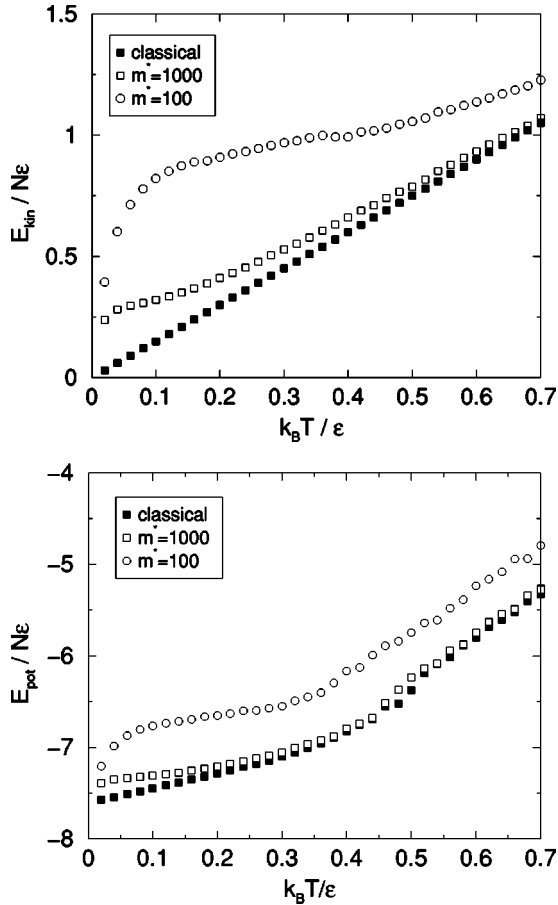


FIG. 17. Kinetic (top) and potential energy versus temperature for pore condensates with $m^* = 1000$ and $m^* = 100$ in a cylindrical pore of radius $R = 3\sigma$ and length $L = 20\sigma$ (150 particles). Comparison of PIMC ($P = 16$) and classical MC simulations.

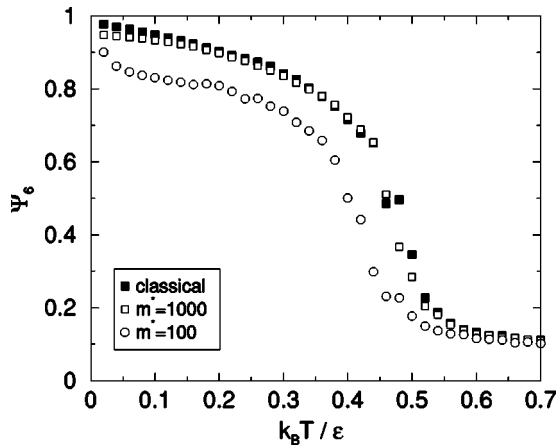


FIG. 18. The bond orientational order parameter of the outer layer of the LJ condensate in a cylindrical pore of radius $R = 3\sigma$ in azimuthal direction versus temperature. Comparison of a classical simulation and results of a PIMC simulation for pore condensates with $m^* = 1000$ and $m^* = 100$ (parameters as in Fig. 17).

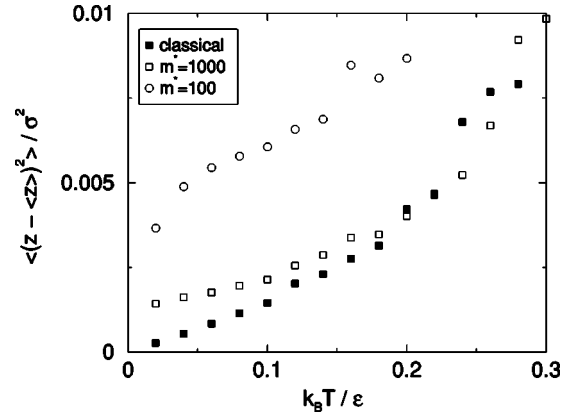


FIG. 19. Average mean square displacement in z direction of condensate particles. Comparison of classical MC simulations and PIMC simulations ($P = 16$) for pore condensates with masses $m^* = 1000$ and $m^* = 100$ in a cylindrical pore of radius $R = 3\sigma$.

higher than in the vicinity of the axis due to quantum delocalization or “broadening” of the particles. This may explain why the structures found in the latter case are similar to those found in classical pores with a radius of 3σ . Since the solid structures in case of $m^* = 100$ are different from those of $m^* = 1000$ and the classical solid structures, the triple point temperature of this system cannot be compared directly.

V. SUMMARY AND CONCLUSIONS

In this paper we have studied structures, phase transitions, and quantum effects in pore condensates by a combination of finite size scaling and path integral Monte Carlo simulation techniques.

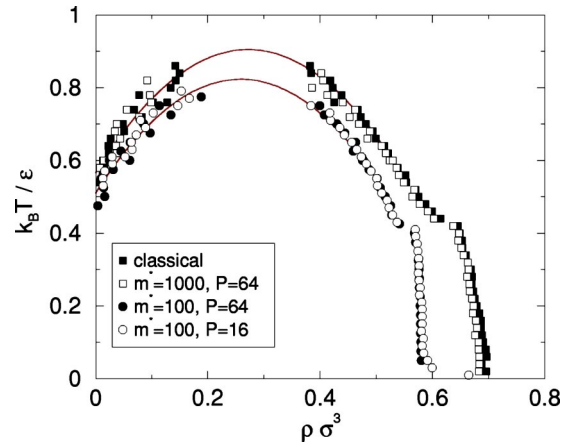


FIG. 20. Comparison of the phase diagram of LJ pore condensates with $m^* = 100$ and $m^* = 1000$ in a cylindrical pore of radius $R = 3.25\sigma$ (MC and PIMC simulations with $P = 16$ and $P = 64$, 300 Particles, length $L = 37.67\sigma$). Lines, quadratic fits (as guide for the eyes) through the data ($k_B T / \epsilon > 0.6$) for $m^* = 100$, $P = 64$ and the classical case.

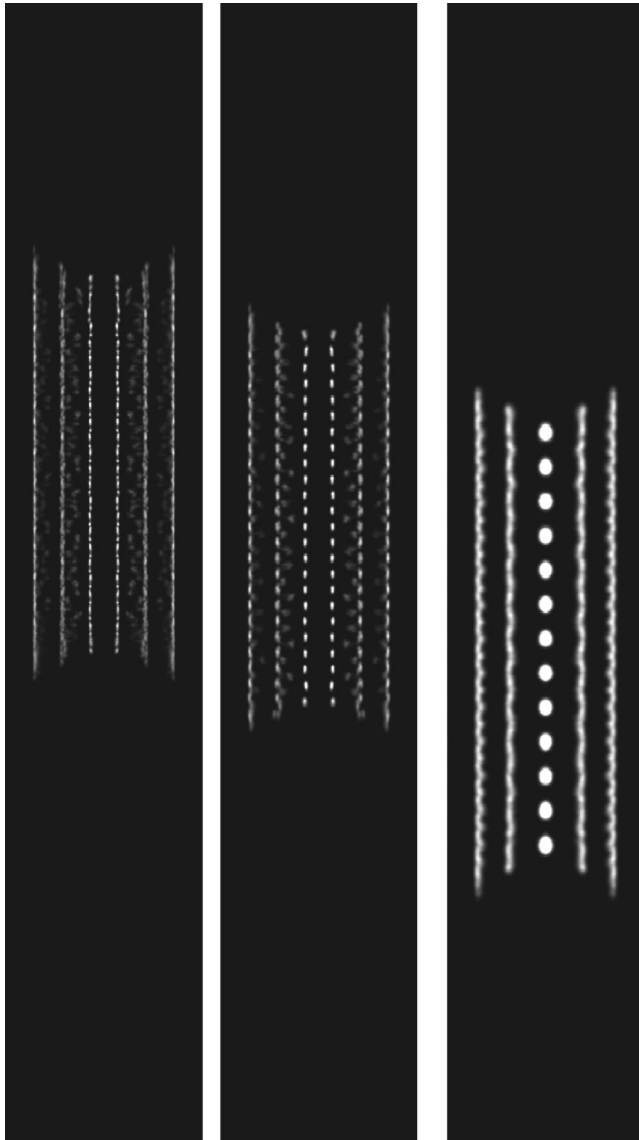


FIG. 21. Density distributions (cylindrical average) for classical LJ condensates in a cylindrical pore of radius $R=3.25\sigma$ at $T^*=0.1$. Comparison of classical MC simulations (left) and PIMC simulations ($P=64$) for $m^*=1000$ (middle) and $m^*=100$ (right) condensates.

The effects of finite pore diameter and the interaction strength between the particles and the cylinder wall on the structures and phase diagrams has been calculated with particular emphasis on the solid structures. Besides reductions of the critical temperature of the adsorbate-condensate transition with decreasing pore diameters several interesting effects on the solidification scenario have been found. For strong particle-wall interactions the system freezes at low temperatures in layers from the cylinder wall towards the pore center, for weak particle-wall interactions solid structures appear locally which are known from the bulk materials. The freezing process may appear in two stages, where parts of the system close to the cylinder wall freeze at a higher temperature than the remainder of the system close to the cylinder axis. For other interaction strengths the adsorbate freezes at a different temperature than the condensate. In recent experiments two stage freezing phenomena have been predicted. In the solid structures meniscus shaped fluid-solid interfaces are found.

Quantum effects on the phase diagrams have been quantified as well. For lighter (Ne) particles the critical temperature and the condensate density are reduced by about 10% compared to the classical case. The quantum ground state oscillations destabilize the system and thus result in lower phase transition temperatures. Structural changes due to the ground state oscillations are found in the solid. As an example the occupancy of sites on the cylinder axis for light particles due to packing effects in contrast to the behavior of systems with heavy particles is analyzed.

As a result of our studies it turns out that a complete overview on solid and fluid structures and phase diagrams in pore condensates at low temperatures can only be obtained by taking into account quantum effects—which can be done efficiently by the PIMC method.

ACKNOWLEDGMENTS

Support by the DFG (Ni-259/8-2), the SFB 513, and granting of computer time from the NIC and the HLRS is gratefully acknowledged.

-
- [1] Z. Zhang and A. Chakrabarti, Phys. Rev. E **50**, R4290 (1994); **52**, 2736 (1995).
 - [2] J.C. Lee, Phys. Rev. Lett. **70**, 3599 (1993).
 - [3] A. Chakrabarti, Phys. Rev. Lett. **69**, 1548 (1992).
 - [4] A.J. Liu and G.S. Grest, Phys. Rev. A **44**, R7894 (1991).
 - [5] A.J. Liu, D.J. Durian, E. Herbolzheimer, and S.A. Safran, Phys. Rev. Lett. **65**, 1897 (1990).
 - [6] L. Monette, A.J. Liu, and G.S. Grest, Phys. Rev. A **46**, 7664 (1992).
 - [7] M.W. Maddox, K.E. Gubbins, M. Sliwinska-Bartkowiak, and Soong-hyuck Suh, Mol. Simul. **17**, 333 (1997).
 - [8] M.W. Maddox, K.E. Gubbins, J. Chem. Phys. **107**, 9659 (1997).
 - [9] R. Radhakrishnan and K.E. Gubbins, Phys. Rev. Lett. **79**, 2847 (1997).
 - [10] L.D. Gelb and K.E. Gubbins, Phys. Rev. E **56**, 3185 (1997).
 - [11] P. Huber and K. Knorr, Phys. Rev. B **60**, 12 657 (1999).
 - [12] L.D. Gelb, K.E. Gubbins, R. Radhakrishnan, M. Sliwinska-Bartkowiak, Rep. Prog. Phys. **62**, 1572 (1999).
 - [13] P. Levitz, G. Ehret, S.K. Sinha, and J.M. Drake, J. Chem. Phys. **95**, 6151 (1991).
 - [14] D. Wallacher and K. Knorr, Phys. Rev. B **63**, 104202 (2001).
 - [15] D.P. Landau and K. Binder, *A Guide to Monte Carlo Simulations in Statistical Physics*, (Cambridge University Press, Cambridge, 2000).
 - [16] R.P. Feynman and A.R. Hibbs, *Quantum Mechanics and Path*

- Integrals* (McGraw-Hill, New York, 1965); H.F. Trotter, Proc. Am. Math. Soc. **10**, 545 (1959); Commun. Math. Phys. **51**, 183 (1976); J.A. Barker, J. Chem. Phys. **70**, 2914 (1979); K.S. Schweizer, R.M. Stratt, D. Chandler, and P.G. Wolynes, *ibid.* **75**, 1347 (1981); D.M. Ceperley, Rev. Mod. Phys. **67**, 279 (1995); P. Nielaba, in *Annual Reviews of Computational Physics V*, edited by D. Stauffer (World Scientific, Singapore, 1997), p. 137.
- [17] G.S. Heffelfinger, F.v. Swol, and K.E. Gubbins, Mol. Phys. **61**, 1381 (1987).
- [18] J. Hoffmann and P. Nielaba, in *High Performance Computing in Science and Engineering '01*, edited by E. Krause and W. Jäger (Springer-Verlag, Berlin, 2002), p. 92.
- [19] J. Hoffmann, Ph.D. thesis, University of Konstanz, 2002, (unpublished) <http://www.ub.uni-konstanz.de/kops/volltexte/2002/810>
- [20] P. Nielaba, in *Computational Methods in Surface and Colloid Science*, edited by M. Borowko (Marcel Dekker, New York, 2000), pp. 77–134.
- [21] M. Presber, D. Löding, R. Martonak, P. Nielaba, Phys. Rev. B **58**, 11 937 (1998).
- [22] M. Reber, D. Löding, M. Presber, Chr. Rickwardt, and P. Nielaba, Comput. Phys. Commun. **121-122**, 524 (1999).
- [23] C. Rickwardt, P. Nielaba, M.H. Müser, K. Binder, Phys. Rev. B **63**, 045204 (2001).